2016 SNMMI Highlights Lecture: General Nuclear Medicine

Patrick M. Colletti, MD, University of Southern California, Los Angeles, CA

From the Newsline Editor: The Highlights Lecture, presented at the closing session of each SNMMI Annual Meeting, was originated and presented for more than 30 years by Henry N. Wagner, Jr., MD. Beginning in 2010, the duties of summarizing selected significant presentations at the meeting were divided annually among 4 distinguished nuclear and molecular medicine subject matter experts. Each year Newsline publishes these lectures and selected images. The 2016 Highlights Lectures were delivered on June 15 at the SNMMI Annual Meeting in San Diego, CA. In this issue we feature the lecture by Patrick M. Colletti, MD, from the University of Southern California (Los Angeles), who spoke on highlights in general nuclear medicine. Note that in the following presentation summary, numerals in brackets represent abstract numbers as published in The Journal of Nuclear Medicine *(2016;57[suppl 2]).*

This year's SNMMI Annual Meeting included multiple presentations on novel chemical constructs for radiopharmaceutical development, with many more topics than can be covered in a brief session such as this. Studies spanned the spectrum from basic science through preclinical testing, and we are clearly seeing the basis for future clinical applications. Given the general encouragement engendered by the recent approvals for ^{18}F-FACBC and ^{68}Ga-DOTATATE, it is hoped that new and innovative radiopharmaceuticals will proceed quickly through the development pipeline to beneficial use in patients.

I will highlight just 2 studies in which investigators developed such novel agents and applied them to proof-of-concept research in animal models. Huang et al. from Stanford University (CA) and the Huazhong University of Science and Technology (Wuhan, China) reported on "Strained cyclooctyne: a multifunctional molecular scaffold for constructing high-performance gastrin-releasing peptide receptor (GRPR)–targeted probes for PET/CT of prostate cancer" [7]. The authors designed and tested a novel platform to facilitate the preparation of high-performance PET probes. Using this platform, they developed ^{68}Ga-labeled bombesin analogs with excellent in vivo imaging properties, fast excretion through the kidneys and liver, and high tumor-to-background ratios in an animal model of prostate cancer (Fig. 1). The result is a promising PET probe for clinical GRPR-targeted imaging in prostate cancer.

Patrick M. Colletti, MD

Zhang et al. from the British Columbia Cancer Agency and Research Centre (Vancouver, Canada) reported on "Melanoma imaging with ^{68}Ga-labeled cyclized alpha–melanocyte stimulating hormone (α-MSH) peptides using PET" [3]. These authors synthesized 3 DOTA-conjugated α-MSH peptides for potential use in melanocortin-1 receptor (MC1R) targeting for imaging and/or radionuclide therapy in metastatic melanoma. Excellent tumor visualization

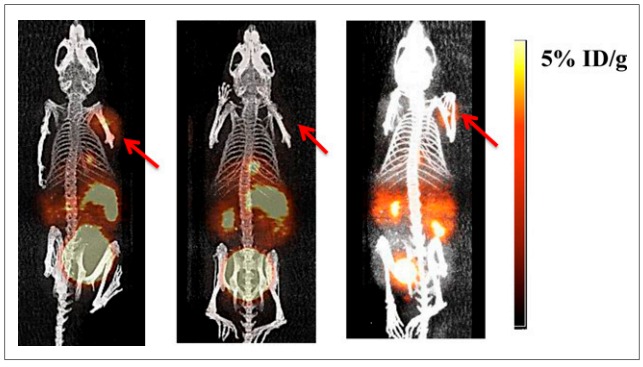

FIGURE 1. ^{68}Ga-NODAGA-based imaging in a rat model of prostate cancer. Left: 2 hours after ^{68}Ga-NODAGA-ZY8 injection; tumor-to-nontumor ratio (T/NT) = 24.57 ± 3.16. Middle: ^{68}Ga-NODAGA-ZY8 with blocking 2 hours after injection; T/NT = 1.76 ± 0.89. Right: 2 hours after ^{68}Ga-NODAGA-JMV594 injection; T/NT = 10.80 ± 0.80.

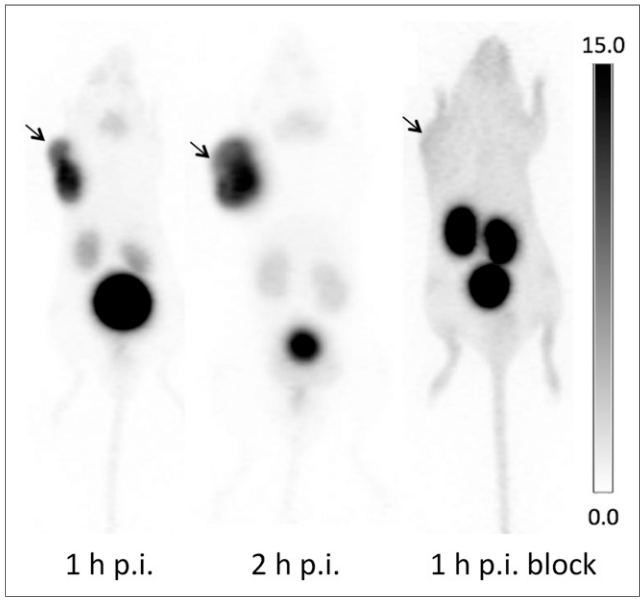

FIGURE 2. Melanocortin-1 receptor targeting for PET imaging in a mouse model of melanoma. Left: 1 hour after injection. Middle: 2 hours after injection. Right: 1 hour after block.

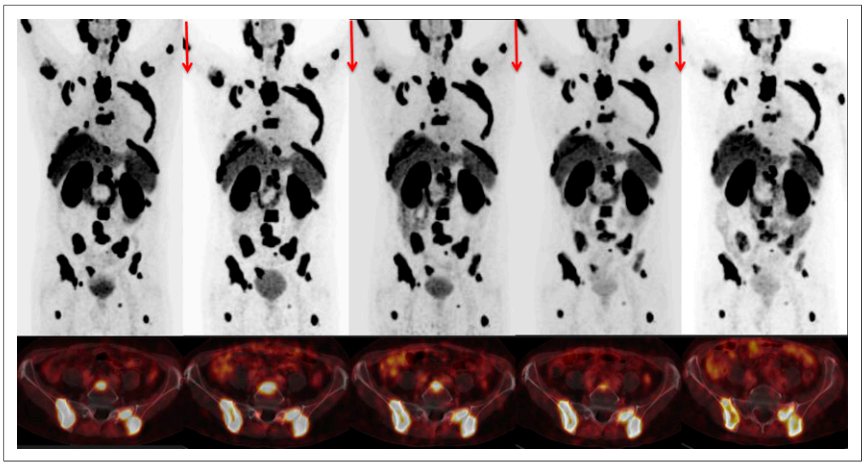

FIGURE 3. ^{177}Lu–prostate-specific membrane antigen I&T in a patient with heavily pretreated metastatic castration-resistant prostate cancer at (left to right) baseline and at 2-, 4-, 6-, and 8-month treatment timepoints. Prostate-specific antigen levels declined from 105 to 14 ng/mL.

and exceptional contrast were achieved with all 3 ^{68}Ga-labeled peptides. In a preclinical model of an MC1R-positive tumor, they showed high uptake in tumor versus background in <60 minutes (Fig. 2). The images show that by 2 hours the tumor-to-background ratio and renal activity were quite low, whereas with a blocking agent renal activity was high. MC1R ligands such as these, then, have the potential for development as theranostic agents for melanoma.

Eiber et al. from the Technische Universität München (Munich and Garching, Germany) reported on "Systemic radioligand therapy with ^{177}Lu–prostate-specific membrane antigen (^{177}Lu-PSMA) I&T in patients with metastatic castration-resistant prostate cancer (MCRPC)" [61]. Twenty-two heavily pretreated patients with MCRPC received up to 4 cycles of the ^{177}Lu-PSMA I&T agent at 8-wk intervals, with ^{68}Ga-PSMA PET/CT after each cycle. The authors showed that although CT imaging results did not change dramatically over the 4 cycles, actual uptake in many patients was significantly lower. The proportions of patients achieving a maximum prostate-specific antigen (PSA) decline of >30%, >50%, and >90% were 56%, 28%, and 11%, respectively. Assessment of bone and soft tissue metastases indicated complete remission in 5%, stable disease in 63%, and progressive disease in 32% of participants. The patient shown in Figure 3 was among those who did quite well clinically, with PSA declining from 105 to 14 ng/mL over the 8-month treatment period.

Chequer et al. from the Hôpital Antoine-Béclère (Clamart, France) and the Hôpital Bichat–Claude-Bernard (Paris, France) reported that "Cardiac denervation evidenced by MIBG occurs earlier than amyloid deposit detection by diphosphonate scintigraphy in patients with a transthyretin familial amyloid polyneuropathy (TTR-FAP)" [8]. The authors assessed the comparative values of detection of amyloid deposits with ^{99m}Tc-diphosphonates and of sympathetic cardiac denervation by ^{123}I-MIBG in 76 consecutive patients with genetically proven TTR-FAP. The delay between diphosphonate and MIBG imaging was 6–12 days. In patients with suspected cardiac involvement, MIBG imaging was abnormal more frequently than diphosphonate imaging. MIBG was abnormal in 45% of cardiac-asymptomatic patients; only half of those with cardiac denervation had a positive diphosphonate scan. The investigators concluded that "this suggests that denervation detected by MIBG is more frequent and earlier than significant amyloid deposits evidenced by diphosphonates." Figure 4 is an example of a patient whose diphosphonate image was negative but in whom ^{123}I-MIBG scintigraphy was positive.

Derlin et al. from the Hannover Medical School (Germany) and the Technische Universität München (Garching, Germany) reported on "Clinical molecular imaging of the chemokine receptor CXCR4 in idiopathic pulmonary

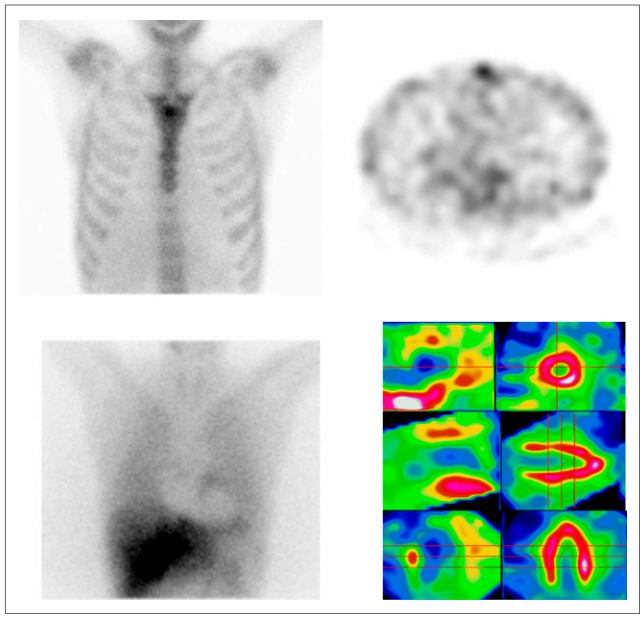

FIGURE 4. ^{99m}Tc-diphosphonate (top) and ^{123}I-MIBG imaging (bottom) in a 39-year-old woman with genetically proven transthyretin familial amyloid polyneuropathy symptomatic for cardiac involvement (left ventricular ejection fraction = 73%). Top: SPECT showed no diphosphonate uptake in the cardiac area. Bottom: ^{123}I-MIBG scintigraphy (left) and simultaneous dual-isotope (right; ^{123}I-MIBG and ^{99m}Tc-MIBI) cardiac CZT camera imaging showed diffuse and heterogeneous denervation.

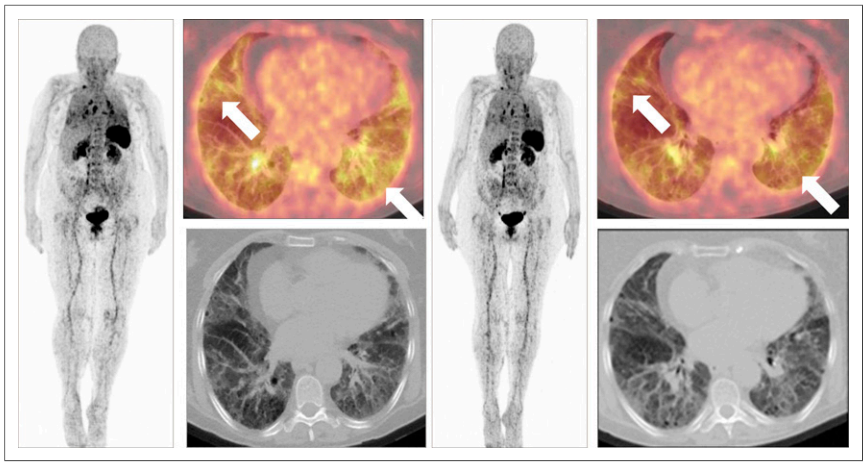

FIGURE 5. ^{68}Ga-pentixafor PET/CT in assessment of pirfenidone treatment of idiopathic pulmonary fibrosis. Example of 59-year-old woman before (left; SUV_{peak} = 3.1, SUV_{mean} = 2.5) and after (right; SUV_{peak} = 2.7, SUV_{mean} = 2.2) therapy.

fibrosis (IPF) using ^{68}Ga-pentixafor PET/CT" [483]. The authors used quantitative PET to evaluate pulmonary CXCR4 expression in 17 IPF patients and compared results with those from high-resolution CT of the chest, lung function tests, and a multidimensional index and staging system. They found that targeted ^{68}Ga-pentixafor imaging identified global and regional CXCR4 expression patterns in lung parenchyma and other organs. CXCR4 upregulation showed interindividual variability and was positively associated with established prognostic imaging and staging assessments. Moreover, pharmacologic intervention with pirfenidone, an approved antifibrotic treatment for IPF, could be shown with ^{68}Ga-pentixafor PET to stabilize or improve lung function in a subset of treated patients. Figure 5 shows results of such treatment in a 59-year-old woman with IPF. Although CT imaging did not show marked improvement, SUV_{peak} and SUV_{mean} on PET were down 10% and 13%, respectively, after treatment. The authors concluded that CXCR4 PET imaging may have a role in monitoring disease activity and response to treatment in IPF.

Meaningful Utilization for PET/MR

Several reports at this meeting provided good examples of effective roles for PET/MR in clinical imaging. As is clear, PET/MR is most useful in those indications in which MR provides better information than CT. Simultaneous PET and MR imaging may be convenient, but it is most useful in those cases in which good superimposition of the images provides additional data and in which dynamic changes are shown. Kogan et al. from Stanford University (CA) reported on "^{18}F-fluoride PET/MR imaging of metabolic bone activity in knee osteoarthritis (OA)" [318]. These investigators used ^{18}F-fluoride PET/MR to characterize osseous metabolic abnormalities in patients with knee OA and to correlate bony MR features with uptake on PET. Their results showed that ^{18}F-fluoride PET provided important metabolic information about subchondral bone remodeling and that simultaneous PET/MR may detect knee abnormalities unseen on MR imaging alone. They suggested that this imaging approach may provide new insights into OA pathogenesis and lead to new treatment targets to arrest onset and progression of OA. Figure 6 shows an example of PET-only images in a reconstructed anterior cruciate ligament (ACL) injury. Figure 7 shows correlations between PET and MR imaging, where different MR sequences are able to clearly bring out subchondral bone changes also visible on PET. The etiology is, of course, that cartilage damage in the knee is associated with a loss of proteoglycans, which leads to an increase in unbound water in the knee joint and in the cartilage itself. This, in turn, leads to changes in T1rho and T2 sequence results. Knee pain, however, does not originate in the noninnervated menisci or the noninnervated chondral cartilage; it comes from the synovium and subchondral bone. The investigators used projection maps of PET/MR data to explore imaging correlations elucidating knee pain in OA (Fig. 8). Bone deposition is apparent, and osteophytes and bone marrow lesions are seen medially and laterally. T1rho and T2 sequences both show areas of increased water, corresponding to OA changes and cartilage thinning.

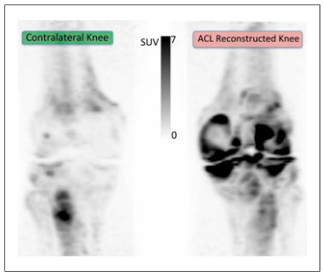

FIGURE 6. ^{18}F-NaF uptake in contralateral (left) and operated (right) knee 1 year after anterior cruciate ligament (ACL) reconstruction. More uptake, indicating subchondral bone remodeling, is seen in the reconstructed knee.

These are the types of physiologic changes that can alter lives. With increased pain comes decreased mobility and the potential for associated morbidities, such as metabolic syndrome. Johansson et al. from Sormland–Uppsala Universitet (Eskilstuna, Sweden), Uppsala University (Sweden), and Uppsala University Hospital (Sweden) reported on "Whole-body assessment of tissue-specific insulin sensitivity using an integrated PET/MR system" [45]. The study included 5 control subjects and 5 individuals with type-2 diabetes who underwent ^{18}F-FDG PET and integrated PET/MR imaging while in a steady-state glucose clamp condition. Kinetic modeling of tissue-specific glucose uptake was performed with Patlak analysis using

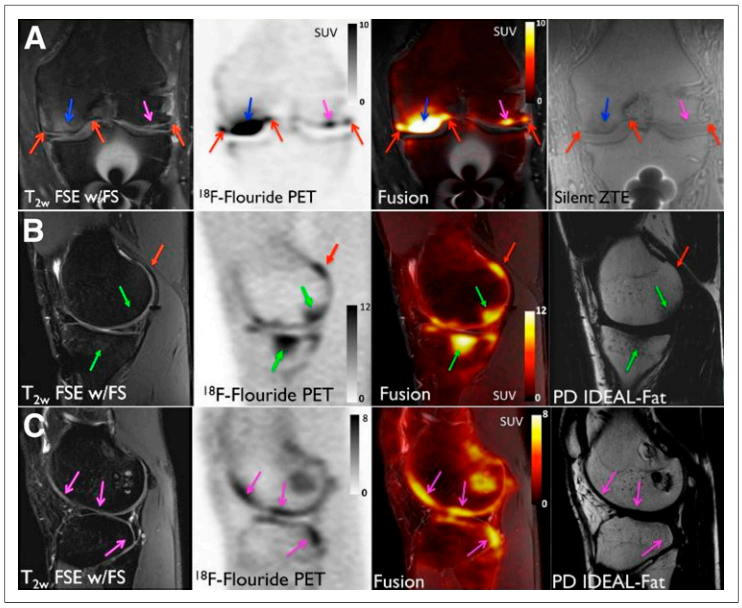

FIGURE 7. Bone marrow lesions (blue arrows), osteophytes (red arrows), and sclerosis (green arrows) findings on MR imaging were correlated with high ^{18}F-NaF uptake on PET. Several regions of high uptake on PET did not correlate with MR findings.

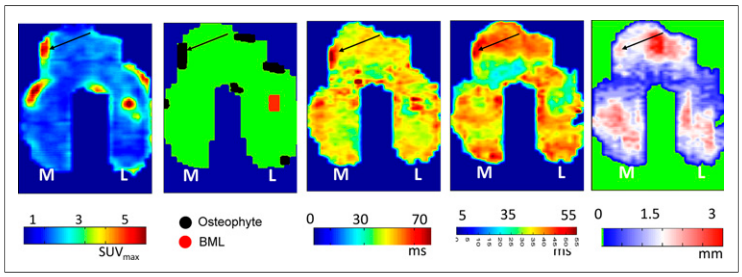

FIGURE 8. Projection maps of PET/MR data with (left to right) PET, osteoarthritis features, T1rho, T2, and cartilage thickness. PET/MR allows simultaneous acquisition of metabolic bone data (PET) with high-resolution tissue morphology and biochemical measures of soft tissue health (MR), facilitating evaluation of early degenerative changes across all tissues in the joint.

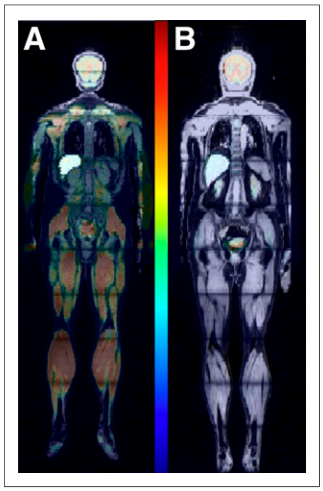

FIGURE 9. Whole-body assessment of tissue-specific insulin sensitivity with ^{18}F-FDG PET. (A) Healthy individual with M value of 15 (mg/kg-minute) with high tissue-specific glucose uptake; and (B) individual with type-2 diabetes with M value of 5 and low tissue-specific glucose uptake.

image-derived input functions (IDIFs). With these data, the investigators created total body maps (Fig. 9) based on an image-derived metric (M value) expressing individual whole-body insulin sensitivity. This whole-body PET/MR protocol for assessing tissue-specific insulin-mediated glucose metabolism has excellent potential and is a novel application for this integrated imaging technology.

In another diabetes-related presentation, Hernandez et al. from the University of Wisconsin Madison reported on "Radio-manganese PET imaging of pancreatic beta cells" [5]. They

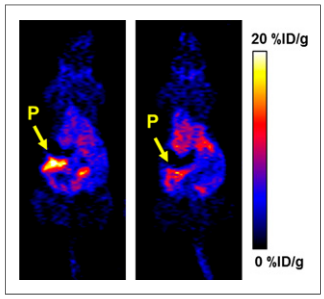

FIGURE 10. ^{52}Mn PET imaging of pancreatic beta cells (P) with (left) glibenclamide stimulant and (right) diazoxide suppressant.

created a mouse model for pancreatic beta cell function, labeled beta cells with ^{52}Mn, and stimulated or suppressed insulin release. Dynamic PET imaging showed fast clearance of the radionuclide from circulation and marked uptake in pancreas, kidneys, heart muscle, thyroid, and liver. When insulin release was stimulated, pancreatic uptake showed significant increases (Fig. 10). The authors noted that "compared to manganese-based MRI methods, ^{52}Mn PET provides improved sensitivity, dynamic range, clearance, and reduced toxicity for beta cell imaging." These and similar models evaluating agents and interventions (even diets) that affect insulin secretion have the potential to yield a broad range of information that can directly affect diabetes treatment and management.